Binder-free 2D MXene/activated carbon for High-performance Supercapacitors and Methylene Blue Adsorption

YUE LI[1], kamdem pascal[1], lanshu xu[1], and xiaojuan jin[1]

[1]Affiliation not available

April 28, 2020

Abstract

we have assembled the 2D MXene flakes and acid activated carbon (AAC) into a 3D sandwich architecture expected to avoid the serious restacking problem of 2D MXene flakes and develop MXene-based functional materials. When used for energy storage, 2D MXene, as a flexible, conductive and electrochemically active binder, furnishes a new perspective and possibility to assemble flexible and conductive electrodes without any current collector, binders or conductive additives. The flexible MXene/AAC 2:1 electrode delivers the specific capacitance of 378 F g-1 at 0.5 A g-1 and a capacitance retention of 88.9% at 30 A g-1. Impressively, asymmetrical supercapacitors have been assembled with MXene/AAC hybrids as positive electrode and delivers exceptional electrochemical properties. The MXene/AAC 2:1//AAC achieves 177 F g-1 at 0.5 A g-1, 97.4% retention after 10000 circles of GCD measurements at 5 A g-1. Moreover, the 3D sandwich architecture of MXene/AAC hybrids with great specific surface exhibits noteworthy absorption

Binder-free 2D MXene/activated carbon for High-performance Supercapacitors and Methylene Blue Adsorption

Yue Li[a],Lanshu Xu[a], Pascal Kamdem[b], Xiao-Juan Jin[a]11*Corresponding author. Tel.: +8613718160441, Fax: None. E-mail address:*jxj0322@163.com*(XiaojuanJin).

[a]MOE Engineering Research Center of Forestry Biomass Materials and Bioenergy, Beijing Forestry University, 35 Qinghua East Road, Haidian, 100083, Beijing, China.

[b] College of Agriculture and Natural Resources, School of Packaging Michigan State University, East Lansing, MI 48864

Abstract: In this work, we have assembled the 2D MXene flakes and acid activated carbon (AAC) into a 3D sandwich architecture which are expected to avoid the serious restacking problem of 2D MXene flakes and develop MXene-based functional materials. When used for energy storage, 2D MXene, as a flexible, conductive and electrochemically active binder, furnishes a new perspective and possibility to assemble flexible and conductive electrodes without any current collector, binders or conductive additives. In the 3D sandwich architecture, the AAC particles are encapsulated between the MXene flakes and enlarge the interlayer space of MXene, significantly perfecting the electrochemical performance. The flexible MXene/AAC 2:1 electrode delivers the specific capacitance of 378 F g^{-1} at 0.5 A g^{-1} and a capacitance retention of 88.9% at 30 A g^{-1}. Impressively, asymmetrical supercapacitors have been assembled with MXene/AAC hybrids as positive electrode and delivers exceptional electrochemical properties. The MXene/AAC 2:1//AAC achieves 177 F g^{-1}at 0.5 A g^{-1}, 97.4% retention after 10000 circles of GCD measurements at 5 A g^{-1}. Moreover, the 3D sandwich architecture of MXene/AAC hybrids with great specific surface exhibits noteworthy adsorption capacity (311.5 mg/g) to remove Methylene blue (MB).

Keywords: MXene, acidified activated carbon, asymmetric supercapacitor, adsorption, Methylene blue

Introduction:

Recently, fast advances of wearable and portable electrochemical capacitors require miniaturized, lightweight, self-powered systems. Currently, flexible supercapacitors, as a new type of energy storage devices, have gained substantial interest in related fields due to their fast charge-discharge rate, high power density and wide temperature operating range and low maintenance cost[1]. Manufacturing electrodes with remarkable mechanical flexibility is the main parament for fabricating flexible supercapacitors[2]. Many researches have focused primarily on using the carbon-based electrode materials for supercapacitors such as carbon nanotubes, carbon aerogels and activated carbon fibers and graphene[3, 4]. Especially activated carbons are the most commonly used owing to their well-developed microstructure, high specific surface area, low cost and relatively high packing density[5-8]. However, activated carbon, as electrode materials requires polymer binders which usually occupy about 10% of the electrode mass without any capacitance contribution and reduce the energy density of supercapacitors[9, 10]. Furthermore, the polymer binders are insulator to electricity, which usually increase the resistance, lowering the power density of devices. Therefore, using activated carbon and conductive additives to fabricate electrodes could increase the electrical conductivity[11]. Flexibility is also a main parament to consider in the as-obtained carbon electrodes. Because the carbon electrodes are rather stiff and could not be employed in flexible devices[12, 13]. To offset this defect, flexible substrates are often employed to add flexibility. The traditional flexible substrates are main carbon nanotubes, graphene and textiles electrodes with thin conductive layers. These additives exhibit relatively low flexibility with lightweight and occupying a large part of the electrode volume[14].

2D nanomaterials, for instance graphene, transition metal dichalcogenides, transition metal oxides/hydroxides and MXene have opened new possibilities in terms of energy storage applications because they could significantly improve the electrochemical properties as binder-free electrodes materials[15, 16]. MXenes, as an emerging family of 2D transition metal carbides and nitrides has opened new possibilities in terms of energy harvesting and storage because they exhibit impressive mechanical performance, high electronic conductivity and exceptional rate capability[15-17]. 2D transition metal carbides MXene are generally produced by selective etching of the A-group (generally, group III A or IV A) element layers from MAX phase precursors with a general formula of $M_{n+1}X_nT_x$, where M is an early transition metal, X is carbon and/or nitrogen, $T_x$denotes surface functional groups such as -OH, -F and/or -O and n is1-3[18-20]. MXene are employing as a promising, versatile platform for energy storage equipment with the combination of hydrophilic surface, noteworthy mechanical stability and metallic conductivity (6000 -8000 S cm^{-1}) which distinguish them from other 2D materials and make them promising candidates for energy storage, transparent conductors, sensor, catalysis and electromagnetic-interference applications[21-23].

However, similar to other 2D nanomaterials, the electrochemical properties of MXenes are impeded by their self-restacking and aggregation during drying and electrode fabrication processes owing to the strong van der Waals interaction between adjacent nanosheets[24, 25], which severely reduced their functions in their corresponding field. To compete the shortcoming, many researches concentrate on introducing interlayer spacers, integrating MXene sheets into 3D structures and creating porous structures, which are proposed to tackle these issues[26, 27]. Typically, Gogotsi's groups have proposed a fabrication of flexible, sandwich-like Mxene/CNT composite paper electrodes through alternating filtration of CNT and MXene dispersion[28]. Gogotsi's groups have prepared MXene/graphene electrode films for outstanding volumetric capacitance by using electrostatic self-assembly between negatively charged MXene and positively charged rGO with rGO inserting in between MXene layers[29].

Herein, we report a novel method to fabricate and assemble flexible electrodes for supercapacitors by exploring $Ti_3C_2T_x$ MXene as the binder,a flexible backbone, a conductive additive and an additional active material. In the as-prepared electrode materials, activated carbon particles are enclosed by MXene layers and could expand the layer distance of the MXene which ensure easy charge and electrolyte infiltration. The MXene layers could enhance flexibility of the hybrids and fabricate a 3D constructive network to speed

up the electronic transmission. When fabricated as the supercapacitors electrode, the as-fabricated flexible MXene/activated carbon hybrids show a superb gravimetric capacitance and outstanding rate properties owing to the rapid ion transport and electron transfer to redox-active sites in the unique 3D conductive network. Besides, some researches have proved that MXene could be applied for wastewater treatment and ion separation as a promising candidate. Mahmoud's groups have fabricated lamellar $Ti_3C_2T_x$ for selective reduction and remediation of $BrO_3^-$from water system. Atieh's groups have prepared the adsorption of barium from natural and produced/co-produced water using Ti_3C_2 nanoparticles as a sorbent material. However, the organic dyestuff such as methylene blue adsorption behavior and mechanism of MXene has not been clear yet. In this research, we have explored the adsorption properties of MXene and revealed its adsorption mechanism. The MXene/activated carbon has an excellent hardness and Young's modulus which revealed their potential use in environmental cleaning, mechanics and energy storage.

2. Materials and Methods

Materials, the preparation of acidified activated carbon and the synthesis of $Ti_3C_2T_x$nanosheets were exhibited in supporting information.

Fabrication of MXene-bonded acidified activated carbon hybrids

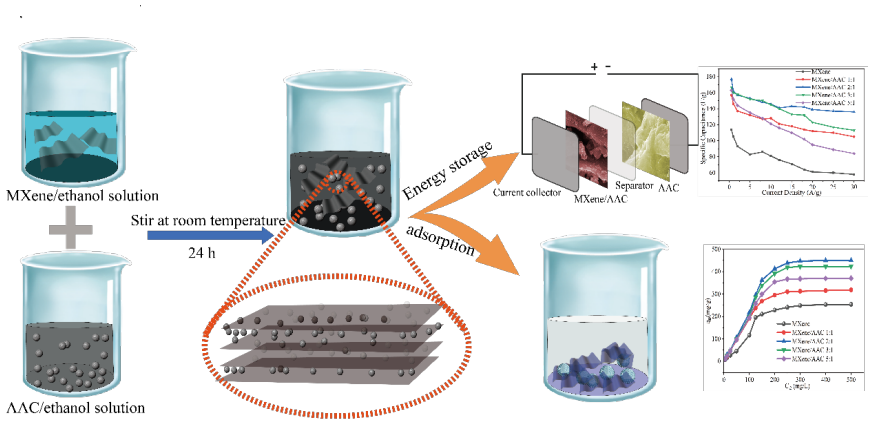

Scheme 1. Schematic of the growth process for MXene/AAC hybrids

Briefly, the aqueous dispersions of MXene and acidified activated carbon particles were mixed at various weight ratios of MXene/acidified activated carbon (1:1, 2:1, 3:1 and 4:1 and 6:1) and then further sonicated for about 30 min to obtain a homogeneoussolution. The mixed solution was vacuum-filtered and thenvacuum-dried at 60 for 6 h to obtain free-standing, flexible film with a diameter of 40 mmm. The films prepared with MXene/acidified activated carbon (1:1, 2:1, 3:1 and 5:1 and were marked as MXene/AAC-1:1, MXene/AAC-2:1, MXene/AAC-3:1 and MXene/AAC-5:1, respectively. For comparison, neat MXene films were fabricated with the same procedures described above and the detailed procedures were discribed in Scheme 1.

Evaluation of methylene blue adsorption properties

Absorption properties and the removal efficiency of MXene/AAC hybrids was conducted and calculated by detecting the adsorbent dosage, initial pH and initial concentration of methylene blue in the aqueous solution. The aqueous liquid was methylene blue-water solution with the concentration of methylene blue ranging from 50 mg/L to 2000 mg/L. For each adsorption experiment, 10 mg MXene/AAC adsorbent was added into a 50 mL methylene blue solution and then ultrasonic-dispersed to form an even and stable solution. The mixtures were oscillated at room temperature for appropriate time intervals ranging from 10 min to 48 h to calculate the kinetic adsorption. After that, the mixture was filtered to remove the residual adsorbent and the methylene blue concentration of the dilute solution was analyzed[30]. The adsorption capacity q_e (mg/g) was calculated by using the following equation:

$q_e = \frac{(C_0 - C_r) \times V}{1000m}$ (1)

The adsorption percentage is calculated as followed equation:

Removel (%) $= \frac{(C_0 - C_r)}{C_0} \times 100$(2)

Where C_0 and C_r are the initial and residual concentrations (mg/L) methylene blue, respectively; V is the solution volume (ml); and m (g) is the adsorbent weight (g).

To confirm the optimum mass of MXene/AAC for maximum removal of methylene blue from the mixture solution, different weight of MXene/AAC hybrids ranging from 5 to 100 mg were tested. All the samples were oscillated at room temperature. To study the effect pH on the removal efficiency of methylene blue, a series of experiments were conducted at different pH values ranging from 2-12 by adjusting with HCl or NaOH. The adsorption performance of the adsorbent regenerated from 1-3 desorption recycles were evaluated, respectively.

Electrochemical measurements

The electrochemical measurements of the fabricated MXene/AAC //activated carbon asymmetric supercapacitor were implemented in 7 M KOH aqueous electrolyte in a three-electrode cell at room temperature. The power density (P) and energy density (E) of the asymmetric supercapacitors were calculated according to the following equation[10, 11]:$C_m = (I^t)/($

The schematic representation shown in Scheme. 1 illustrates the process of sandwich-like MXene/AAC composite. First, a thin layer of MXene, as a flexible and conductive binder, is formed using vacuum-assisted filtration of a colloidal solution containing delaminated suspended $Ti_3C_2T_3$ flakes. Then, a layer of AAC is deposited on the top of $Ti_3C_2T_3$ layer. Finally, the sandwich-like MXene/AAC composite is produced by repeating the process. The procedure is much simpler than the conventional paste electrode fabrication means by mixing the Polytetrafluoroethylene (PTFE) as the binder, Acetylene black as the conductive binder and the active materials in aqueous solution, then coating the slurry onto nickel foam current collectors[5, 11].

Fig.1. FESEM and TEM images of MXene/AAC: (a-i): FESEM images of MXene/AAC 2:1 (j-l): TEM images of MXene/AAC 2:1.

The morphology and microstructure of synthetic MXene/AAC 2:1 are observed by Field emission electron microscope (FESEM)(Fig.1.a-i) at different magnifications and the corresponding energy-dispersive spectrometry (EDS) mapping (Fig S1 (c)). As shown in Fig.1. (a-c), the MXene/AAC hybrids have a sandwich-like structure, where the AAC powers are evenly encapsulated in the MXene flakes, which could effectively avoid MXene flakes stacking and could improve the electrochemical property. The MXene exhibits a separately lamellar and accordion-like structure with lateral size of 0.5-2 μm and the AAC particles are relatively rigid and irregular with the size of 10 nm-1μm shown in Fig.1. (d-i), demonstrating that LiF and HCl treatment effectively removed Al ion from the lattices. The EDS mapping of C, Ti, O and N exhibited in Fig. S1(c). It is obviously observed that C and Ti are uniformly distributed as a whole, without visible boundaries. The sandwich-like structure with the encapsulation of the AAC particles and MXene flakes in the MXene/AAC hybrids is further confirm by TEM shown in Fig.1. (j-l) and Fig. S1(a-b), respectively. The Fig.S2 shows that the MXene/AAC film are flexible, freestanding and could be directly employed as electrodes for supercapacitors without the any metal current collector.

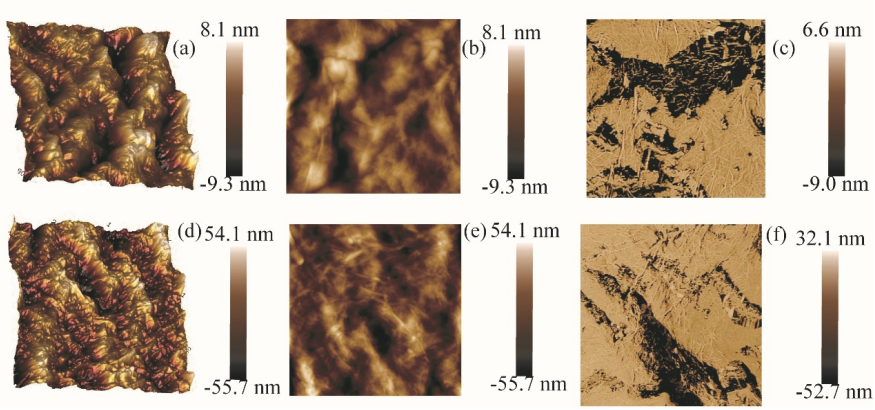

Fig.2. AFM images of MXene and MXene/AAC 2:1 (a-c) AFM images of MXene; (d-f) AFM images of MXene/AAC 2:1

To further observe the morphology and microstructure of synthetic and MXene and MXene/AAC 2:1, the atomic force microscope (AFM) is employed and shown in Fig.3. (a-f). As shown in Fig.3. (a-c), the pure MXene flakes are curved and folded, evident of their flexible characteristic. The pure MXene shows a densely stacked morphology with the interlayer spacing of 17.4 nm. As shown in Fig.3. (d-f), with the intercalation of AAC, the MXene/AAC 2:1 exhibits much increased thickness due to their loose structure as well as the low density of the porous carbon. The interlayer spacing of MXene/AAC 2:1 is enlarged with a thickness of 109.8 nm, as well as the porosity of AACs which could provide additional and faster diffusion paths for electrolyte ions during rapid charge/discharge processes and enhances the accessibility of MXene flakes to electrolyte ions, resulting in an improved rate property when employed as supercapacitance electrodes.

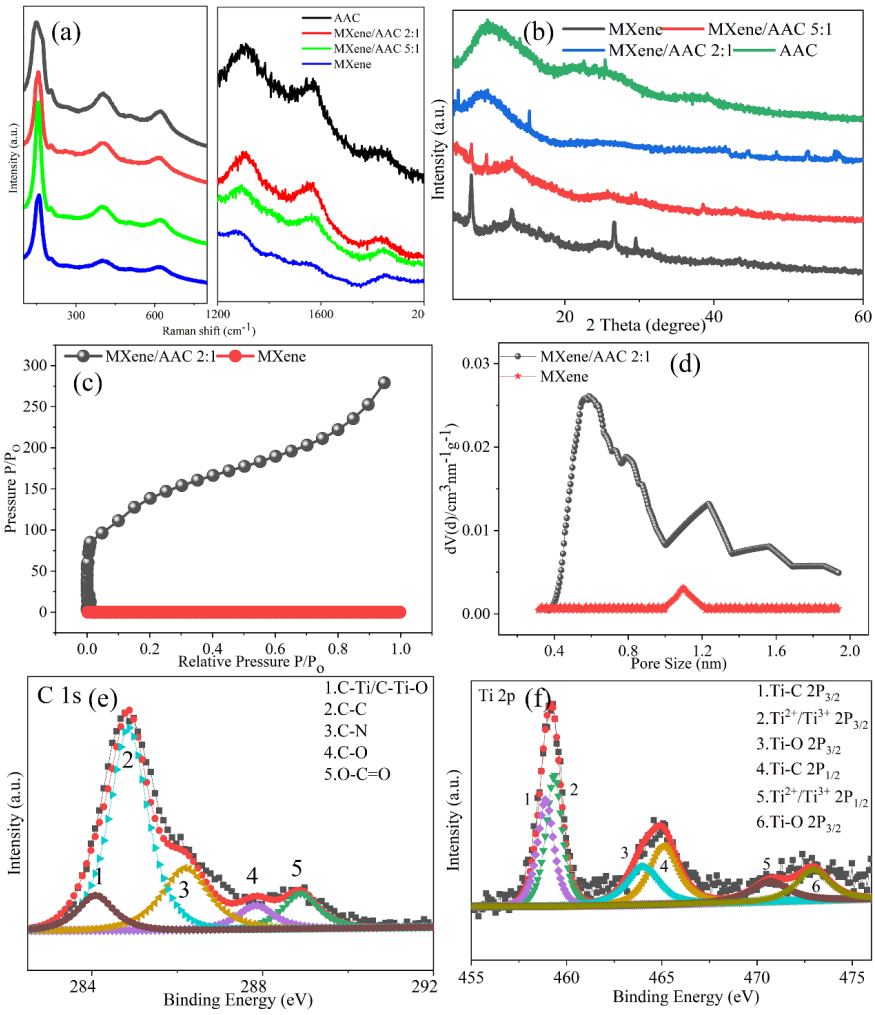

Fig.3. (a) Raman spectra of MXene, MXene/AAC and AAC; (b) XRD imaged of MXene, MXene/AAC and AAC; (c) Nitrogen adsorption isotherms of MXene and MXene/AAC 2:1; (d) Pore size distribution of MXene and MXene/AAC 2:1; (e) C 1s spectra of MXene/AAC 2:1;(f) Ti 2p spectra of MXene/AAC 2:1

In order to confirm that the enhanced interlayer spacing observed in ATM is statistically significant. X-ray diffraction (XRD) patterns are performed for pure MXene, MXene/AAC 5:1, MXene/AAC 2:1 and AAC composites and shown in Fig.3. (b). The MXene film exhibits a peak (002) at about 2ϑ=7.5°, corresponding to d-spacing values of 12.62 Å. The peaks corresponding to the (002) plane of MXene/AAC 2:1 and MXene/AAC 5:1 downshift to about 2ϑ=7.06° and 2ϑ=6.07° which demonstrates a 3.0 Å and 4.2 Å in the c -lattice parameter (c -LP) and 1.5 Å and 2.1 Å increase the d -spacing, respectively. In the pure AAC, a broad peak at 2ϑ=25° is observed, demonstrating exceptional graphitization, which further proved the stability of the composite after chemical treatment. In addition, the intensity of (002) peaks decreases with the increase of AAC content, indicating that the order between MXene layers is interrupted due to hybridization with AAC. Besides, all MXene/AAC composites have the broad peak (002) of AAC particles which confirms manufacturing of MXene/AAC. However, the intercalation of AAC into MXene layers could reduce material density and electrical conductivity. As shown in Table S1. The MXene composite has an electrical conductivity of 3206 S cm^{-1} and a material density of 2.01 g cm^{-3}. Nevertheless, the electrical conductivity and material density decrease with the increase of AAC mass ratio. Besides, the MXene/AAC 2:1 and MXene/AAC 5:1 exhibit a quite low material density of 0.309 and 0.406 g cm^{-3} with the electrical

conductivity of 191 and 357 S cm^{-1}, respectively. In contrast, with the increase of AAC mass ratio, the specific surface area (BET) and specific volume (V_{total}) of MXene/AAC increase. The pure MXene shows a much lower BET (18.92 m^2g^{-1}) and V_{total}(0.008 cm^3g^{-1}) than MXene/AAC 2:1 hybrid (1651 m^2g^{-1} and 1.07 cm^3g^{-1}). Due to the large surface areas and abundant specific volume, the electrochemical performance of MXene/AAC are greatly enhanced.

The microstructure and exposed surface area of the as-prepared hybrid are examined by the nitrogen (77K) adsorption-desorption measurement. Fig.3. (c-d) show the nitrogen adsorption isotherms and pore size distributions of pure MXene and MXene/AAC 2:1. The MXene/AAC 2:1 particles present a combination of type-I and type-II isotherms, demonstrating that the microporous-mesoporous structure which could be ascribed to the incorporation of AAC between MXene layers. Fig.3. (a) presents Raman spectra of the pure MXene and MXene/AAC composite. The Raman spectra of MXene and MXene/AAC are similar in the range of 100 to 800 cm^{-1}. The MXene has a sharp peak at about 150 cm^{-1} and broad peaks at about 370 cm^{-1} and 619 cm^{-1}, which are distinctive feature of MXene. On the other hand, the peaks at about 1275 and 1572 cm^{-1} represent as the D-band and G-band, respectively which are signatures of carbon and confirm the incorporation of MXene and AAC. The D-band corresponds to defects and relates to zone boundary k -point phonons and the G-band is due to collective symmetric stretching of sp^2 carbon lattice. The ratio of the D-band and G-band (I_D/I_G) which proportional to the defect sites in graphitic carbon is 1.29 which could calculate the corresponding sp^2 crystallite size to be 9.8 nm according to the followed formula.

$$L_a\,(\mathrm{nm}) = 560/E^4_{\mathrm{laser}}(\tfrac{I_D}{I_G})^{-1} \quad (6)$$

Where L_a is the average sp^2 crystallite size,E_{laser} is the laster excitation energy in eV.

In order to further investigate the mechanism and chemical compositions of synthesized MXene/AAC interaction, X-ray photoelectron spectroscopy (XPS) was employed to examine the chemical composition and surface electronic states and the corresponding images exhibited in Fig.3. (c-d) and Fig. S3 (a-c). The XPS survey spectra as shown in Fig. S3 (a) demonstrate that the MXene/AAC hybrids are mainly composed of C, Ti, O, N and F. High-resolution XPS spectrum in the Ti 2p region (Fig.3. (d)) core levels of MXene/AAC 2:1 hybrids could be deconvoluted into six peaks with components corresponding to Ti-C, Ti(II), Ti(III) and Ti-O peaks. The Ti 2p core level can be fitted with three doublets (Ti $2p_{3/2}$-Ti $2p_{1/2}$) which in agreement with other papers(尚). The Ti $2p_{3/2}$ components mainly located at binding energy of 458.6, 459.1, 463.3 and 464.9 eV correspond to Ti-C $2p_{3/2}$, Ti-O $2p_{3/2}$, C-Ti-T_x $2p_{1/2}$ and Ti-O $2p_{1/2}$, respectively, demonstrating the interaction between MXene and AAC particles at the sites of oxygen dangling bonds. However, the XRD spectrum exhibits no peaks for TiO_2.The Raman pattern of MXene/AAC exhibits similar vibrations in the shift range 100-800 cm^{-1}, demonstrating that the appearance of Ti-O peak mainly comes from the MXene-to-AAC contact area[31, 32]. The C 1s core level (Fig.3. (c)) could be fitted with five components at binding energy of 284.1, 284.8, 286.3, 286.6, and 288.9 eV, which could be assigned to C-Ti-O, Ti-O, C-C, C-N, C-O and O=C-O bonds, respectively. confirming the interaction between MXene layers and AAC particles[33, 34]. Fig.S3. (b) exhibits the N 1s core level mainly centered at binding energy of 397.6, 398.8 and 399.9 eV which could be accordingly assigned to Ti-N, pyridinic N and pyrrolic N, respectively. Fig.S3. (c) exhibits the O 1s core level which could be fitted with three components at binding energy of 530.4, 531.8 and 532.9 eV which further confirm the interaction between MXene flake and AAC particles. The result is in good agreement with the TEM observation.

3.1 Electrochemical capacitive performance

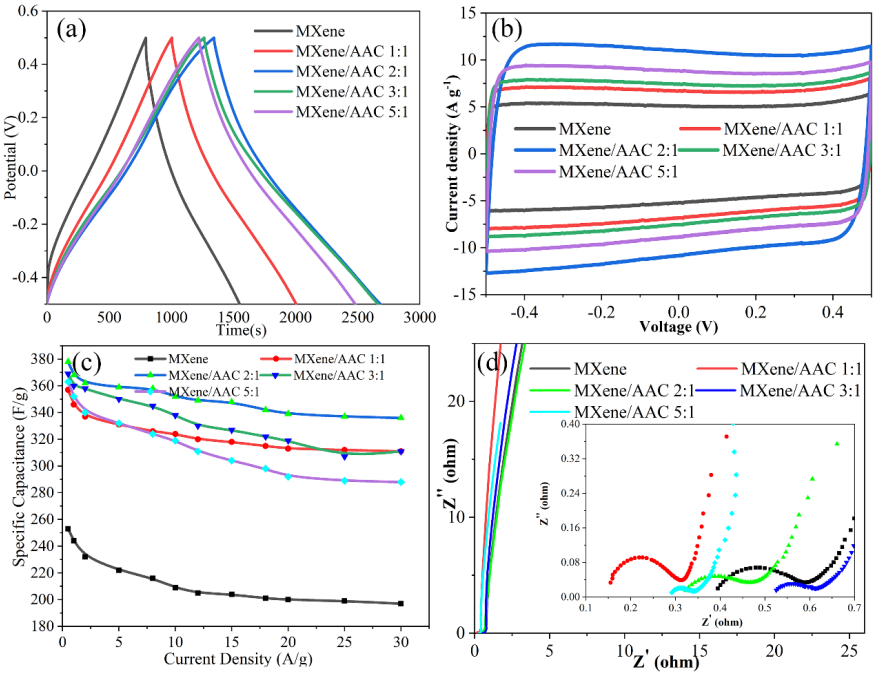

Fig.4. Electrochemical property of pure MXene and MXene/AAC hybrids electrodes: (a) The GCD curves of MXene/AAC hybrids electrodes with various mass ratios at the current density of 0.5 A g^{-1} (b) CV curves of MXene/AAC hybrids electrodes with various mass ratios at the scan rate of 0.1 V s^{-1} (c) specific capacitance of MXene/AAC hybrids electrodes with various mass ratios at different current densities (d) Nyquist plots of MXene/AAC hybrids electrodes with various mass ratios in 7 M KOH in the frequency range from 10^{-2} to 10^{5} Hz

MXene/AAC composites present exceptional mechanical strength, enhanced interlayer spacing, high porosity and conductivity which could be directly employed as the flexible supercapacitance electrodes without any conducting additive and binding agent[33-36]. Therefore, they are expected to possess enhanced electrolyte accessibility, noteworthy rate capability and high volumetric capacitance. The electrochemical properties of the as-obtained MXene/AAC hybrids are examined using a three-electrode system in 6 M KOH aqueous electrolyte. Fig.4. (a) exhibits the galvanostatic charge-discharge (GCD) curves of pure MXene and MXene/AAC hybrids electrodes at 0.5 A g^{-1}. The GCD images have triangular profiles without obvious plateaus and distinct voltage drop in all charge-discharge images, demonstrating the ideal electric double layer capacitors of pure MXene and MXene/AAC. Obviously, the MXene/AAC 2:1 shows the longest discharge time among all the MXene/AAC electrodes, indicating the highest specific capacitance. Fig.S4 (a) reveals GCD curves of MXene/AAC 2:1 at different current densities ranging from 0.5 to 15 A g^{-1}. The nonlinear charge/discharge curves with negligible voltage drop even at 15 A g^{-1} further state clearly the excellent performance of electric double layer and small internal resistance of MXene/AAC 2:1 electrode. The specific capacitances of pure MXene and MXene/AAC are calculated and the corresponding numerical value are exhibited in Fig.4. (c). The specific capacitance of pure MXene (253 F g^{-1}) is much lower than MXene/AAC electrodes (357 F g^{-1} of MXene/AAC 1:1, 378 F g^{-1} of MXene/AAC 2:1, 369 F g^{-1} of MXene/AAC 3:1, 363 F g^{-1} of MXene/AAC 5:1) because of the lower of AAC content which results in the restacked MXene layer. The restacked MXene flakes with inadequate AAC powers adverse to electrolyte infiltration and ion transport, resulting in poor rate capabilities. According to our precious, the specific capacitance of AAC electrode is 264 F g^{-1} due to its high specific surface area[9]. The specific capacitances of MXene/AAC electrodes based on the total mass of MXene/AAC hybrids increase with the increase of AAC mass ratio due to the enhanced BET and pore volume of MXene/AAC hybrids and the enlarged distance between the

MXene layers opened by AAC powers. However, when the mass proportion of AAC and MXene increase from 1:2 to 1:1, the material density decreases from 0.309 to 0.216 g cm^{-1}, the MXene/AAC hybrids exhibit loose structures even could not shape a membrane. MXene/AAC hybrids exhibits increased rate capability even at 15 A g^{-1} better than pure MXene electrode. When the current density increases from 0.5 A g^{-1} to 15 A g^{-1}, the MXene/AAC 2:1 exhibits the best rate capability with the capacitance retention of 88.9%, which is higher than those of MXene/AAC 1:1(87.1%), MXene/AAC 3:1(84.3%), MXene/AAC 5:1(79.3%) and pure MXene (77.8%). The enhanced rate properties of the MXene/AAC electrodes attribute to the 3D sandwich structure constructed by MXene and AAC. The cyclic voltammograms (CVs) of the pure MXene and MXene/AAC hybrids electrodes are presented in Fig.4. (b). It is obviously noted that the shape of the CV profiles at 100 mV s^{-1} for all MXene and MXene/AAC electrodes are nearly rectangular and the CV curve of MXene/AAC 2:1 electrode exhibits the utmost scanning area, indicating the low contact resistance and ideal charge propagation. Fig.S4 (b) exhibits CV images of MXene/AAC 2:1 electrode at different scan rates. The CV curves remain rectangle even at 5 V s^{-1} which is the excellent characterization for the porous carbon-based electrode.

The electrochemical impedance spectroscopy (EIS) measurement is employed in 7.0 M KOH over the frequency range from 0.01 Hz to 100 KHz and presented in Fig.4.(d). It is state clearly that all the Nyquist plots include a similar semicircle in the high-frequency range and an observed straight line in the low frequency region responding to the diffusion-controlled Warburg impedance. Obviously, the semicircles in the high-frequency range for MXene/AAC 2:1 electrode are relatively smaller than other electrodes prepared under same preparation which reveal MXene/AAC 2:1 electrode has a smaller resistance and fast/easy transfer of electrons/ions to the inlayer of the material. This is possibly because Further confirm MXene/AAC 2:1 electrode is favorable for electrolyte to increase the kinematic velocity of ions through the surface of the active materials, thus increasing the contactable area between the electrolyte and electrode[37].

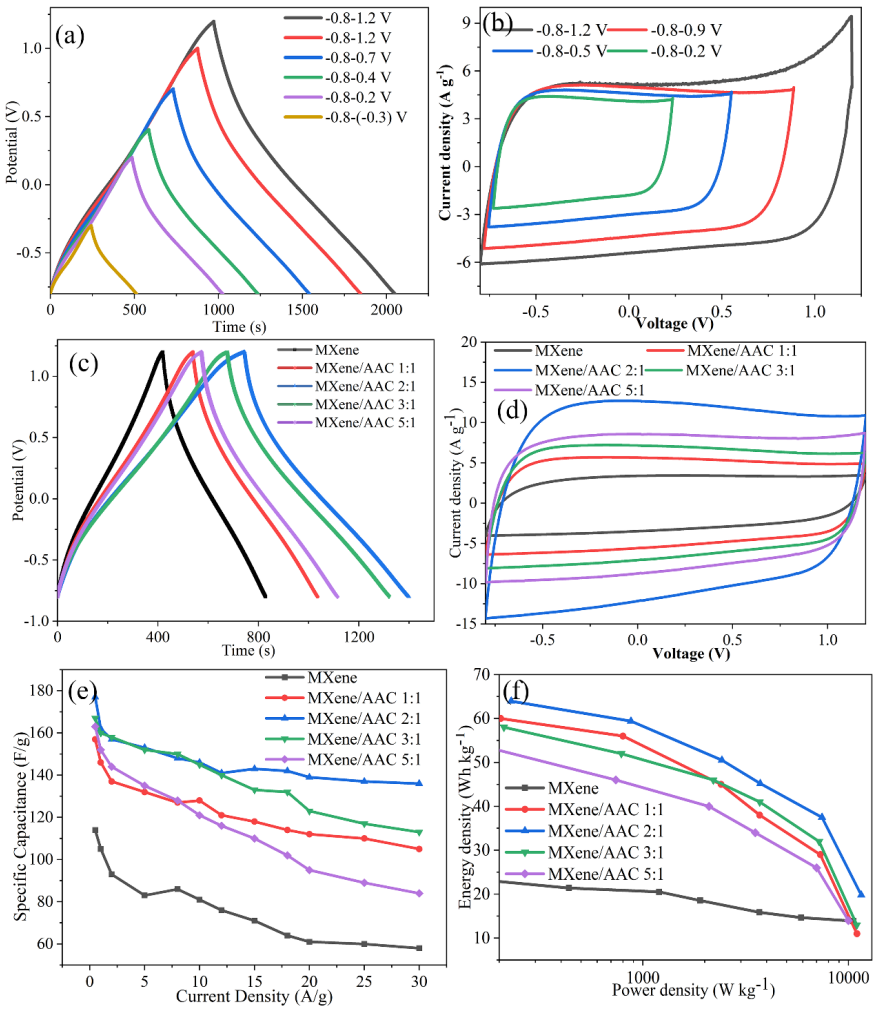

Fig.5. (a) GCD curves of the MXene/AAC 2:1//AAC asymmetrical capacitances at 0.1 A g^{-1} at different voltage (b) GCD curves of the MXene/AAC 2:1//AAC asymmetrical capacitances at 0.1 mV s^{-1} at different voltage (c) The GCD curves of MXene/AAC hybrids asymmetrical capacitances with various mass ratios at the current density of 0.5 A g^{-1} (d) CV curves of MXene/AAC hybrids asymmetrical capacitances with various mass ratios at the scan rate of 0.1 V s^{-1} (e) specific capacitance of MXene/AAC hybrids asymmetrical capacitances with various mass ratios at different current densities (f) Ragone plot for energy density and power density.

In order to further investigate the capacitive efficiency of pure MXene and MXene/AAC electrodes for practical application, we have successfully fabricated asymmetrical capacitances using MXene/AAC hybrids as positive electrode and AAC as the negative electrode in 7.0 M KOH solution. In order to determine the working voltage window of MXene/AAC, GCD and CV images of MXene/AAC 2:1//AAC asymmetrical capacitances are measured. As shown in Fig.5. (a), the GCD images shows ideal capacitive property in the voltage window from -0.8-(-0.3) V to -0.8-1.2 V. Furthermore, GCD curves of MXene/AAC 2:1//AAC asymmetrical capacitances in the voltage range of -0.8-1.2 V at different current densities shown in Fig.S4 (c) exhibits symmetric shapes demonstrate exceptional reversibility and outstanding coulombic efficiency. After a series of experimental measurements and study, an operating voltage window from -0.8 V to 1.2 V was selected to research the electrochemical properties of the MXene/AAC//AAC devices. Fig.5. (b) exhibits the CV images of the synthesized MXene/AAC2:1//AAC at different working voltage windows from -0.8-(-0.3)

V to -0.8-1.2 V at the scan rate of 100 mV s^{-1}. Obviously, the stable voltage could range from -0.8 V to 1.2 V with no noticeable sharp current increase due to obvious oxygen evolution, which might originate from the electrolyte decomposition/water splitting. The GCD images of pure MXene//AAC and MXene/AAC//AAC devices at the current density of 100 mA g^{-1} shown in Fig.5. (c) have triangular shape without apparent voltage drop, suggesting the ideal electric double layer properties. The specific capacitances of pure MXene//AAC and MXene/AAC//AAC devices are calculated at various current densities and the corresponding images are shown in Fig.5. (e). The specific capacitance of MXene//AAC asymmetrical capacitor (114 F g^{-1}) is lower than those of MXene/AAC//AAC (157 F g^{-1} of MXene/AAC 1:1//AAC, 177 F $g^{-1}$of MXene/AAC 2:1//AAC, 167 F g^{-1} of MXene/AAC 3:1//AAC, 163 F g^{-1} of MXene/AAC 1:1//AAC). Besides, when the current density increases from 0.5 A g^{-1} to 15 A g^{-1}, the MXene//AAC exhibits the minimum rate retention of 49.58%, which is lower than those of MXene/AAC1:1//AAC (66.88%), MXene/AAC2:1//AAC (76.84%), MXene/AAC3:1//AAC (67.66%) and MXene/AAC5:1//AAC (51.55%). In addition, the repetitive charge-discharge cycling of MXene//AAC and MXene/AAC2:1//AAC exhibit noteworthy cycling stability shown in Fig.S5, about 88.6% and 97.4% of the initial capacity are retained after 10000 circles of GCD measurements at the current density of 5 A g^{-1}, respectively.

Fig.5. (d) exhibits the CV images of pure MXene//AAC and MXene/AAC//AAC devices. The quasi-rectangular CV shapes, reflecting an excellent symmetry and capacitance characteristics.

The Ragone curve of MXene//AAC and MXene/AAC//AAC for energy density (E, Wh kg^{-1}) and power density (P, kW kg^{-1}) in a voltage window of -0.8-1.2 V at different current densities is illustrated in Fig.5. (f). The expansion of voltage window beyond 2 V is one of the main factor for improving the electrochemical performance as energy and power density increase with the square of the potential window. The specific energy density of MXene//AAC and MXene/AAC2:1//AAC decreased from 23.89 Wh kg^{-1} to 13.89 Wh kg^{-1} and from 63.95 Wh kg^{-1} to 19.8 Wh kg^{-1} based on the total mass of active material. Nevertheless, the power density has raised from 0.112 kW kg^{-1} to 5.89 kW kg^{-1} and from 0.23 kW kg^{-1} to 11.55 kW kg^{-1} at the current density ranging from 1 to 15 A g^{-1}. The excellent electrochemical properties for energy storage could be comparable to reported similar systems, as shown in Table 1.

Table 1. Comparison of obtained results with reported similar systems

Composite	Electrolyte	Potential Window /V	Specific capacitance /F g^{-1}	Energy density /Wh kg^{-1}	Power density/KW kg^{-1}	Cyclic stability	Ref
MXene/carbon nanotube	1M (EMITFSI)	2	320 at 2 mV s^{-1}	—	—	90% after 1000	Ref[38]
MXene/GN	K_2SO_4	0.95	370 at 5 A g^{-1}	—	—	-	Ref[39]
PEDOT/$Ti_3C_2T_x$	1 M $LiClO_4$/acetonitrile	0.6	2.4 mF cm^2 at 10 mV s^{-1}	8.7	0.55	90% after 10000	Ref[40]
MXene-rGO	6 M KOH	1	-	8.6 mW h cm^{-3}	0.2 W cm^{-3}	97% after 10000	Ref[41]
AC/MXene	organic electrolyte	0.5	126 at 0.1 A g^{-1}	—	—	—	Ref[14]
MXene/PANI	3 M H_2SO_4	0.6	336	—	—	98% after 2000	Ref[42]
MXene/AAC	7 M KOH	1	378 F g^{-1}	63.95	0.23	97.4% after 10000	In this work

3.2 Methylene blue adsorption behavior and the mechanism

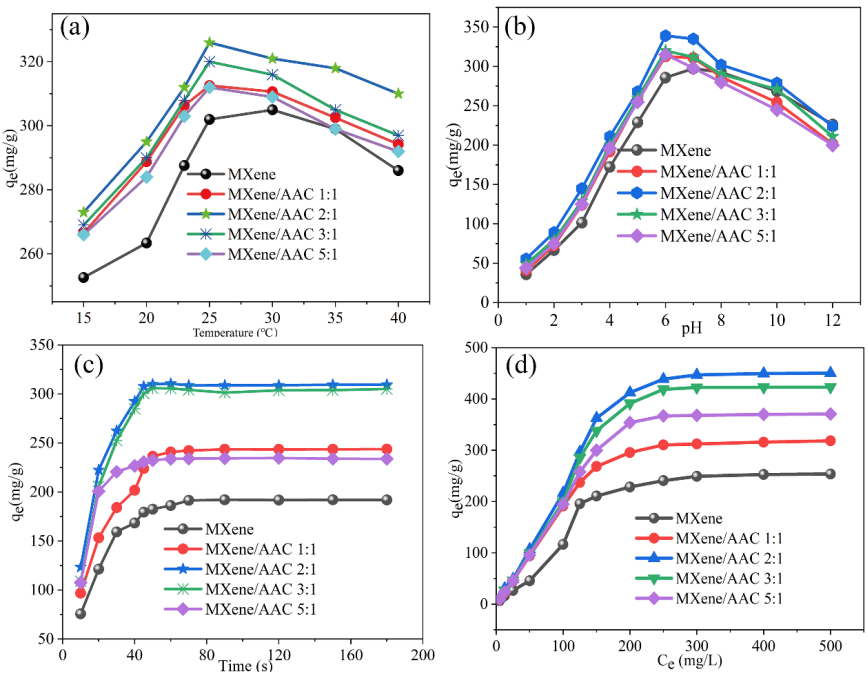

Fig.6. (a) Effect of temperature on adsorption capacity (b) Effect of pH on adsorption capacity (c) Plot of the MB removal rate and time for different adsorbents (d) Adsorption isotherms of MB on pure MXene and MXene/AAC hybrids

The MXene/AAC could not only possess merits of 3D sandwich structure, but also presents hydrophilia, great specific surface area, chemical stabilities and noteworthy electrical conductivity, which endows MXene/AAC hybrids promising candidates for wastewater treatment. To further explore and understand possible application, the adsorption property of pure MXene and MXene/AAC hybrids is explored to research the adsorptive removal of methylene blue from wastewater.

The effects of initial solution temperature and pH on MB adsorption are researched within the temperature range from 15 to 40 and pH range between 1 to 12 and the corresponding imagines shown in Fig.6. (a-b). The adsorption capacities of MB show an obvious increase, such as the adsorption capacitance of MXene/AAC 2:1 adsorbent increased from 55.6 mg/g to 335 mg/g with the increase of pH in the range of 1-7. Similarly, the pure MXene and MXene/AAC hybrids exhibit the highest adsorption capacities when the temperature is 25. Adsortion isotherms of MB on pure MXene and MXene/AAC are shown in Fig.6. (d). MXene/AAC 2:1 exhibits the highest MB adsorption capacity, achieving ca. 343 mg/g. This could be explained that the compact and restacked MXene flakes with inadequate AAC, resulting in poor ion transport and electrolyte infiltration when the mass proportion of MXene and AAC over 2:1. Fig.6. (c) exhibits variation of methylene blue removal rate *vs* . time for pure MXene and MXene/AAC hybrids. The adsorption capacity of pure MXene and MXene/AAC hybrids is evaluated with increasing the adsorption time from 10 to 180 min. The MXene/AAC 2:1 exhibits the highest adsorption capacities (311.5 mg/g) at 180 min among all MXene/AAC and MXene adsorbents (189.4 mg/g for MXene, 243.8 mg/g for MXene/AAC 1:1, 305.1 mg/g for MXene/AAC 3:1, 233.8 mg/g for MXene/AAC 5:1). Actually, pure MXene and MXene/AAC hybrids have achieved a high adsorption capacity nearly as same as the equilibrium adsorption capacities. The high adsorption capacities maybe mainly ascribe to the great specific surface area and oxygen-containing functional groups of AAC which provided some ion-change sites by cation substitution. The oxygen-containing functional groups are prone to adsorb cationic dyes as followed equations:

$$[Ti-O]^{-}H^{+}+\mathrm{MB}^{+}\rightarrow[Ti-O]^{-}\mathrm{MB}^{+}+H^{+}(7)$$

$$[Ti-O]^{-}M^{+}+\mathrm{MB}^{+}\rightarrow[Ti-O]^{-}\mathrm{MB}^{+}+M^{+}(8)$$

The adsorption kinetics of pure MXene and MXene/AAC are examined using the pseudo-first-order and pseudo-second-order kinetics models as followed formulas:

$$\ln(q_e-q_t)=lnq_e-k_1t\ (9)$$

$$\frac{t}{q_t}=\frac{1}{k_2q_e^2}+\frac{t}{q_e}\ (10)$$

Where $q_{\ e}$ (mg/g) represents the equilibrium adsorption capacity, $q_{\ t}$ (mg/g) represents the adsorption capacity at any time, $k_{\ 1}$(min^{-1}) and $k_{\ 2}$ (g $mg^{-1}min^{-1}$) are the pseudo-first-order and pseudo-second-order rate constant, respectively. The kinetic parameters $k_{\ 1}$,$k_{\ 2}$, q_e and correlation coefficients (R^2) are determined by linear regression exhibited in Table S2. It is obviously observed that the experimentally measured data to the pseudo-first-order are not consistent with low correlation coefficients (R^2) (ranging from 0.526 to 0.831). On the contrary, the R^2 is much higher than 0.831 demonstrating that data are well in agreement with pseudo-second-order which is calculated according to Fig.S6 and Fig.S7. The better agreement of the pseudo-second-order model than the pseudo-first-order model indicates that the MB adsorption over the pure MXene and MXene/AAC adsorbents mainly depends on the adsorbent concentration in the MB solution.

4. Conclutions :

In conclusion, we have demonstrated a simple method to encapsulate AAC particles into MXene flakes, shaping a 3D sandwich architecture which are expected to avoid the serious restacking problem of 2D MXene flakes. Besides, the AAC particles with great specific surface area are encapsulated between the MXene flakes and enlarge the interlayer space of MXene. When employed as a binder-free electrode for supercapacitors, the MXene/AAC hybrids exhibits noteworthy electrochemical performance, expecially the MXene/AAC 2:1 electrode. The MXene/AAC 2:1 electrode delivers the specific capacitance of 378 F g^{-1} at 0.5 A g^{-1} and a capacitance retention of 88.9% at 30 A g^{-1}. Besides, asymmetrical supercapacitors have been fabricated using MXene/AAC hybrids as positive electrode and exhibits exceptional electrochemical properties. The MXene/AAC 2:1//AAC achieves a high energy density of 63.95 Wh kg^{-1} at the power density of 0.23 kW kg^{-1} and a 97.4% retention after 10000 circles of GCD measurements at 5 A g^{-1}. In addition, great specific surface exhibits noteworthy adsorption capacity (311.5 mg/g) to remove Methylene blue (MB).

5. Acknowledgements

The authors gratefully acknowledge the financial support of National Natural Science Foundation of China (31470605). And thanks for the support of Chinese Scholarship Council (CSC)

6. References

1. M. Boota and Y. Gogotsi, *Advanced Energy Materials* , 2019,**9** .

2. Y. Dall'Agnese, P. L. Taberna, Y. Gogotsi and P. Simon, *J Phys Chem Lett* , 2015, **6** , 2305-2309.

3. A. K. Fard, G. McKay, R. Chamoun, T. Rhadfi, H. Preud'Homme and M. A. Atieh, *Chemical Engineering Journal* , 2017, **317** , 331-342.

4. J. Fu, L. Li, J. M. Yun, D. Lee, B. K. Ryu and K. H. Kim,*Chemical Engineering Journal* , 2019, **375** .

5. Y. Li, C. Cheng, Y. Yang, X. Dun, J. Gao and X.-J. Jin, *Journal of Alloys and Compounds* , 2019, **798** , 764-772.

6. Y. Li, L. Cui, M. Jia, L. Xu, J. Gao and X. Jin, *New Journal of Chemistry* , 2019, **43** , 5592-5602.

7. Y. Li, M. Jia, L. Xu, J. Gao, F. Zhang and X.-J. Jin, *New Journal of Chemistry* , 2018, **42** , 10733-10740.

8. Y. Li, L. Xu, J. Gao and X. Jin, *RSC Advances* , 2017,**7** , 39024-39033.

9. Y. Li, T.-X. Shang, J.-M. Gao and X.-J. Jin, *RSC Advances* , 2017, **7** , 19098-19105.

10. Y. Li, L. Xu, M. Jia, L. Cui, X. Liu and X. Jin, *Materials & Design* , 2020, **186** .

11. Y. Li, L. Xu, M. Jia, L. Cui, J. Gao and X.-J. Jin, *Journal of The Electrochemical Society* , 2018, **165** , E303-E310.

12. L. Guo, X. Wang, Z. Y. Leong, R. Mo, L. Sun and H. Y. Yang,*FlatChem* , 2018, **8** , 17-24.

13. J. Halim, S. Kota, M. R. Lukatskaya, M. Naguib, M.-Q. Zhao, E. J. Moon, J. Pitock, J. Nanda, S. J. May, Y. Gogotsi and M. W. Barsoum,*Advanced Functional Materials* , 2016, **26** , 3118-3127.

14. L. Yu, L. Hu, B. Anasori, Y.-T. Liu, Q. Zhu, P. Zhang, Y. Gogotsi and B. Xu, *ACS Energy Letters* , 2018, **3** , 1597-1603.

15. Q. Jiang, N. Kurra, K. Maleski, Y. Lei, H. Liang, Y. Zhang, Y. Gogotsi and H. N. Alshareef, *Advanced Energy Materials* , 2019, DOI: 10.1002/aenm.201901061.

16. K. Kim, Y. Ando, A. Sugahara, S. Ko, Y. Yamada, M. Otani, M. Okubo and A. Yamada, *Chemistry of Materials* , 2019, **31** , 5190-5196.

17. X. Wang, T. S. Mathis, K. Li, Z. Lin, L. Vlcek, T. Torita, N. C. Osti, C. Hatter, P. Urbankowski, A. Sarycheva, M. Tyagi, E. Mamontov, P. Simon and Y. Gogotsi, *Nature Energy* , 2019, **4** , 241-248.

18. Q. Tao, M. Dahlqvist, J. Lu, S. Kota, R. Meshkian, J. Halim, J. Palisaitis, L. Hultman, M. W. Barsoum, P. O. A. Persson and J. Rosen,*Nat Commun* , 2017, **8** , 14949.

19. Z. Wei, Z. Peigen, T. Wubian, Q. Xia, Z. Yamei and S. ZhengMing,*Materials Chemistry and Physics* , 2018, **206** , 270-276.

20. X. Xie, M.-Q. Zhao, B. Anasori, K. Maleski, C. E. Ren, J. Li, B. W. Byles, E. Pomerantseva, G. Wang and Y. Gogotsi, *Nano Energy* , 2016, **26** , 513-523.

21. Q. Jiang, N. Kurra, M. Alhabeb, Y. Gogotsi and H. N. Alshareef,*Advanced Energy Materials* , 2018, **8** .

22. M. Laurans, K. Dalla Francesca, F. Volatron, G. Izzet, D. Guerin, D. Vuillaume, S. Lenfant and A. Proust, *Nanoscale* , 2018,**10** , 17156-17165.

23. N. Kurra, B. Ahmed, Y. Gogotsi and H. N. Alshareef, *Advanced Energy Materials* , 2016, **6** .

24. P. Srimuk, F. Kaasik, B. Krüner, A. Tolosa, S. Fleischmann, N. Jäckel, M. C. Tekeli, M. Aslan, M. E. Suss and V. Presser, *Journal of Materials Chemistry A* , 2016, **4** , 18265-18271.

25. L. Yu, Z. Fan, Y. Shao, Z. Tian, J. Sun and Z. Liu, *Advanced Energy Materials* , 2019, **9** .

26. N. Li, X. Chen, W. J. Ong, D. R. MacFarlane, X. Zhao, A. K. Cheetham and C. Sun, *ACS Nano* , 2017, **11** , 10825-10833.

27. J. Luo, W. Zhang, H. Yuan, C. Jin, L. Zhang, H. Huang, C. Liang, Y. Xia, J. Zhang, Y. Gan and X. Tao, *ACS Nano* , 2017, **11** , 2459-2469.

28. M. Q. Zhao, C. E. Ren, Z. Ling, M. R. Lukatskaya, C. Zhang, K. L. Van Aken, M. W. Barsoum and Y. Gogotsi, *Adv Mater* , 2015,**27** , 339-345.

29. J. Yan, C. E. Ren, K. Maleski, C. B. Hatter, B. Anasori, P. Urbankowski, A. Sarycheva and Y. Gogotsi, *Advanced Functional Materials* , 2017, **27** .

30. J. Dai, X. Xiao, S. Duan, J. Liu, J. He, J. Lei and L. Wang,*Chemical Engineering Journal* , 2018, **331** , 64-74.

31. P. A. Rasheed, R. P. Pandey, K. Rasool and K. A. Mahmoud,*Sensors and Actuators B: Chemical* , 2018, **265** , 652-659.

32. J. Shi, S. Wang, Q. Wang, X. Chen, X. Du, M. Wang, Y. Zhao, C. Dong, L. Ruan and W. Zeng, *Journal of Power Sources* , 2020,**446** .

33. R. P. Pandey, K. Rasool, P. Abdul Rasheed and K. A. Mahmoud,*ACS Sustainable Chemistry & Engineering* , 2018, **6** , 7910-7917.

34. Y.-Y. Peng, B. Akuzum, N. Kurra, M.-Q. Zhao, M. Alhabeb, B. Anasori, E. C. Kumbur, H. N. Alshareef, M.-D. Ger and Y. Gogotsi, *Energy & Environmental Science* , 2016, **9** , 2847-2854.

35. M. Hu, C. Cui, C. Shi, Z. S. Wu, J. Yang, R. Cheng, T. Guang, H. Wang, H. Lu and X. Wang, *ACS Nano* , 2019, **13** , 6899-6905.

36. A. S. Levitt, M. Alhabeb, C. B. Hatter, A. Sarycheva, G. Dion and Y. Gogotsi, *Journal of Materials Chemistry A* , 2019, **7** , 269-277.

37. F. Malchik, N. Shpigel, M. D. Levi, T. S. Mathis, A. Mor, Y. Gogotsi and D. Aurbach, *Journal of Materials Chemistry A* , 2019,**7** , 19761-19773.

38. Y. Dall'Agnese, P. Rozier, P.-L. Taberna, Y. Gogotsi and P. Simon,*Journal of Power Sources* , 2016, **306** , 510-515.

39. T. Shang, Z. Lin, C. Qi, X. Liu, P. Li, Y. Tao, Z. Wu, D. Li, P. Simon and Q. H. Yang, *Advanced Functional Materials* , 2019,**29** .

40. J. Li, A. Levitt, N. Kurra, K. Juan, N. Noriega, X. Xiao, X. Wang, H. Wang, H. N. Alshareef and Y. Gogotsi, *Energy Storage Materials* , 2019, **20** , 455-461.

41. C. Couly, M. Alhabeb, K. L. Van Aken, N. Kurra, L. Gomes, A. M. Navarro-Suárez, B. Anasori, H. N. Alshareef and Y. Gogotsi,*Advanced Electronic Materials* , 2018, **4** .

42. A. VahidMohammadi, J. Moncada, H. Chen, E. Kayali, J. Orangi, C. A. Carrero and M. Beidaghi, *Journal of Materials Chemistry A* , 2018,**6** , 22123-22133.